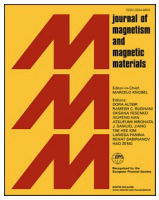
Journal of Magnetism and Magnetic Materials 648 (2026) 174050



Contents lists available at ScienceDirect

Journal of Magnetism and Magnetic Materials

journal homepage: www.elsevier.com/locate/jmmm



Hysteresis-free high linear response and noise characteristic of GMR sensor using pulse width modulation (PWM)-domain wall displacement

Kosuke Komuro [a,*], Arata Kawamura [a], Hirofumi Suto [b], Tomoya Nakatani [b], Daiki Oshima [a], Takeshi Kato [a,c]

[a] Graduate School of Engineering, Nagoya University, Nagoya 464-8603, Japan
[b] Research Center for Magnetic and Spintronic Materials, National Institute for Materials Science, Tsukuba 305-0047, Japan
[c] Institute of Materials and System for Sustainability, Nagoya University, Nagoya 464-8603, Japan

ARTICLE INFO

Keywords:
Magnetic field sensors
Giant magnetoresistance
Pulse width modulation
Domain walls
Linearity
Noise

ABSTRACT

This study examines the output characteristics and noise behavior of giant magnetoresistance (GMR) magnetic field sensors employing the pulse-width modulation domain wall displacement (PWM-DWD) method. In this approach, a high-frequency (up to 100 kHz) sinusoidal magnetic field is applied along the easy axis of the free-layer magnetization in the GMR device to induce oscillatory motion of domain walls, with the modulation amplitude exceeding the coercivity of the free layer. By periodically driving the domain walls close to magnetization saturation, hysteresis in the sensor output is effectively suppressed, thereby yielding a highly linear sensor response. The sensor demonstrated a minimum detectivity of 14 nT/Hz$^{1/2}$ at 120 Hz under a modulation field of 1.1 mT at 100 kHz. The dominant noise source was identified as the stochastic nature of domain wall displacement, and further noise reduction is anticipated through lowering the coercivity of the free-layer material and increasing the modulation frequency.

1. Introduction

Magnetic sensors play a crucial role in a wide range of industries, and their market has been rapidly expanding with advances in autonomous vehicles and the emergence of Internet of Things (IoT) technologies. Among the various types of magnetic sensors that have been developed, such as Hall sensors [1], superconducting quantum interference devices (SQUIDs) [2,3], fluxgate sensors [4–6], and magneto-impedance sensors [7,8], magnetoresistance (MR) sensors have attracted significant attention owing to their simple two-terminal resistor structure, high sensitivity, ease of fabrication, and compatibility with micro-integration processes.

Over the past few decades, MR sensors have been widely applied in numerous fields, including hard disk drive (HDD) read heads [9,10], position encoders [11–13], and current sensors for automotive applications [14,15]. More recently, MR sensors have also been investigated for biomedical applications. For example, giant magnetoresistance (GMR) devices have been utilized in bio-magnetic sensors for cancer detection [16,17]. In this approach, magnetic nanoparticles (MNPs) are functionalized to bind to target cancer cells, and MR sensors detect cancer tissues by sensing the stray fields from MNPs [18–21]. As another example, magnetic tunnel junction (MTJ) sensors have been applied to magnetocardiography (MCG) [22], which monitors heart activity by detecting magnetic fields generated by cardiac electrical currents. Owing to the wide dynamic range of MTJs, MCG measurements outside magnetically shielded rooms have been reported [22], which is not feasible with SQUIDs. Similarly, magnetoencephalography (MEG) detects magnetic fields generated by neural currents beneath the scalp [23]. To realize such medical and biological applications, sensors must achieve detectivity below 1 nT and exhibit stable operation with minimal output hysteresis.

One approach to enhance detectivity is the use of magnetic flux concentrators (MFCs) placed adjacent to GMR or MTJ elements, which can both amplify output signals and reduce noise [24,25]. For instance, MTJ sensors with MFCs have demonstrated noise levels of 940 fT/Hz$^{1/2}$ at 1 Hz [26], and GMR sensors with MFCs achieved 3 pT/Hz$^{1/2}$ at 1 Hz [27]. In these methods, however, sensors typically detect fields along the hard axis of the free layer, which inherently limits sensitivity. To overcome this limitation, we have focused on detecting magnetic fields along the easy axis to enhance output signals. Furthermore, we have applied

* Corresponding author.
E-mail addresses: komuro.kosuke.h2@s.mail.nagoya-u.ac.jp, komuro.kosuke20@gmail.com (K. Komuro), kato.takeshi.i6@f.mail.nagoya-u.ac.jp (T. Kato).

https://doi.org/10.1016/j.jmmm.2026.174050
Received 14 October 2025; Received in revised form 11 March 2026; Accepted 20 March 2026
Available online 26 March 2026
0304-8853/© 2026 The Authors. Published by Elsevier B.V. This is an open access article under the CC BY-NC license (http://creativecommons.org/licenses/by-nc/4.0/).

the domain wall displacement (DWD) technique to GMR sensors, in which the magnetization of the free layer is modulated by oscillating domain walls at high frequency [28,29]. We previously confirmed that the sensitivity increases with the modulation amplitude [28]. In addition, by introducing current-field feedback into DWD sensors [30,31], we improved output linearity and realized a minimum detectivity of 300 pT/Hz$^{1/2}$ at 10 Hz without MFCs [32]. Nevertheless, in conventional DWD sensors, the modulation field amplitude was kept below the coercivity of the free layer, causing the domain structures to be influenced by unintended external fields, which resulted in poor output reproducibility and fluctuations in noise levels. To address these issues, we introduce the pulse-width modulation domain wall displacement (PWM-DWD) technique. The key difference from the conventional DWD approach is that the modulation field amplitude exceeds the coercivity of the GMR free layer. The PWM-DWD sensor detects magnetic fields based on the timing of resistance changes in the GMR device, similar to the operating principle of fluxgate sensors. Although only a few studies have reported on MR sensors operated in PWM mode [33,34], these studies demonstrated that PWM effectively reduces hysteresis in the sensor output. However, the modulation frequency in these works was fixed at approximately 100 Hz, and systematic investigations of the dependence of sensor output and noise spectra on modulation frequency and amplitude were not conducted.

In this study, we investigate the output and noise characteristics of PWM-DWD sensors by varying both the amplitude and frequency of the modulation field. Our results show that the PWM-DWD technique effectively enhances the linearity of the sensor output and suppresses 1/f magnetic noise, yielding flat noise spectra in the low-frequency region. Finally, we demonstrate a minimum detectivity of 14 nT/Hz$^{1/2}$ at 120 Hz under a modulation field of 1.1 mT at 100 kHz.

2. Working principle of PWM sensors

2.1. Modulation method

Fig. 1 (a) and (b) illustrate the schematic resistance curves of a GMR device when an external field H_{ext} is applied along the easy axis of the free layer in the GMR element. As in Fig. 1 (a), a sufficiently large modulation field amplitude H_{mod} was applied along the easy axis to saturate the free layer. Compared to the conventional DWD sensor previously reported in Ref. [32], where H_{mod} was 0.1 mT, the present PWM-DWD sensor uses the increased H_{mod} of approximately 1 mT. This periodic saturation causes the GMR resistance to switch between high and low states, producing a square waveform, and the duty ratio defined as the duration ratio between high and low levels depends on the external field H_{ext}. For example, when $H_{ext} = 0$, the duty ratio is 50% as shown by the red dotted line in Fig. 1 (c). If the finite H_{ext} is applied, it changes the duty ratio of GMR resistance as shown in Fig. 1 (b) and (c). Therefore, the present PWM-DWD sensor detects H_{ext} by observing the duty ratio just as the conventional fluxgate sensor [4,5]. Since the duty ratio will change linearly with H_{ext}, the output signal V_{out} is expected to exhibit small hysteresis.

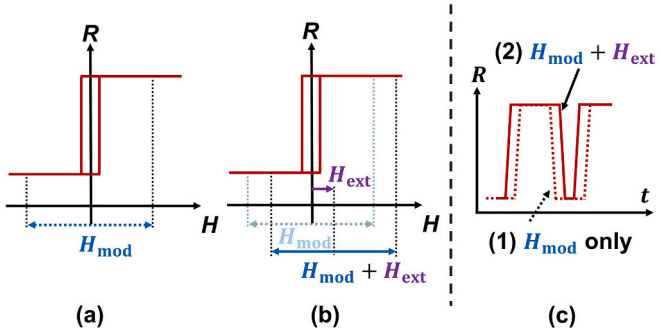


Fig. 1. Working principle of PWM-DWD modulation. (a) H_{mod} saturates the resistance of GMR periodically, and the duration ratio between the high and low resistances takes 50% when $H_{ext} = 0$. (b) If the finite H_{ext} is applied, the duration ratio of the high and low resistances changes. (c) Typical waveform of the resistance of GMR under $H_{ext} = 0$ (dotted line) and finite value (solid line) expected from Figs. (a) and (b).

A schematic of the waveform of V_{out} and the total fields ($H_{mod} + H_{ext}$) applied to the GMR device is shown in Fig. 2. T, t_+, and t_- indicate the period of the modulation field and the durations of the high and low states of the V_{out} waveform, respectively. $\pm H_c$ represent the positive and negative coercive fields required to reverse the magnetization of the free layer. Here, a triangular waveform was assumed for the modulation field, and a square hysteresis loop was assumed for the free layer in the GMR device. The duty ratio of V_{out} is evaluated using the average output voltage (V_{ave}), which can be analytically expressed as follows:

$$V_{ave} = \frac{V_s t_+ - V_s t_-}{T} = \frac{V_s \cdot H_{ext}}{H_{mod}}, \quad (1)$$

where V_s is the absolute value of saturation voltage of V_{out}. One may note that V_{out} exhibits bipolar waveform although resistance of GMR is unipolar. This is because the GMR device is inserted in a bridge circuit followed by instrumentation amplifier, which is described in Sec. 2.3. The eq. (1) indicates that V_{ave} is not affected by hysteresis of the free layer, which results in the highly linear sensor output as will be shown in this paper. In addition, V_{ave} is proportional to $1/H_{mod}$.

2.2. Device Preparation

To realize the PWM detection of H_{ext} described in the previous section, GMR spin-valves were deposited under a magnetic field of 27 mT

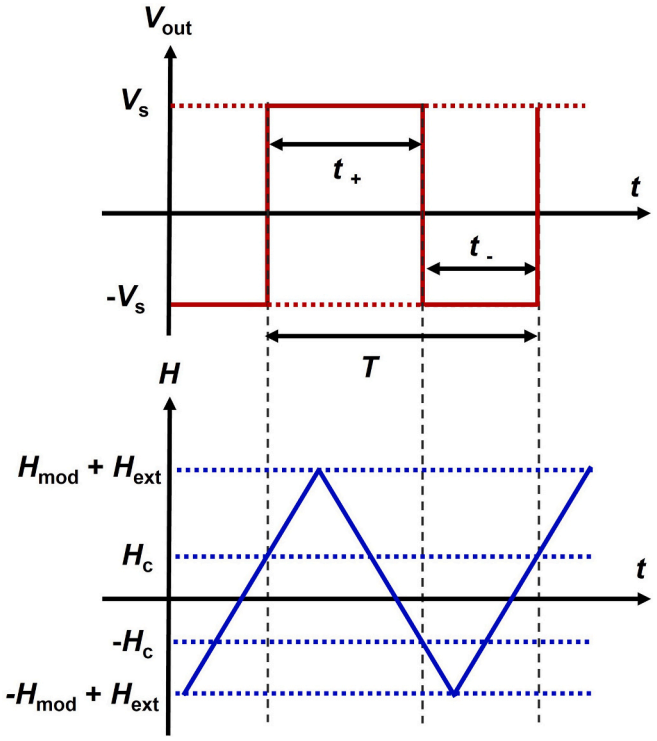


Fig. 2. Schematic of the V_{out} waveform (red) and total fields (H_{mod} + H_{ext}) applied to GMR device (blue). In this figure, it is assumed a triangular waveform of H_{mod}, and a square hysteresis loop of the free layer in GMR device. H_c indicates the coercivity of the free layer, and V_s is the saturation voltage of V_{out}. From the assumptions, the sensor output (the average of the V_{out} waveform) is found to be independent of H_c and proportional to $1/H_{mod}$. (For interpretation of the references to colour in this figure legend, the reader is referred to the web version of this article.)

using our RF magnetron sputtering system to induce uniaxial magnetic anisotropy. As in Fig. 3 (a), the deposited stacks were SiO_2 substrate / Ta (5) / $Ni_{80}Fe_{20}$ (10) / Cu (4) / $Co_{90}Fe_{10}$ (3) / $Mn_{80}Ir_{20}$ (8) / Ta (2), where the numbers in parentheses represent the thicknesses of each layer in nanometers. In the stacks, the $Ni_{80}Fe_{20}$ layer works as a free layer, and the $Co_{90}Fe_{10}$ layer is a pinned layer, where the pinned layer magnetization is stabilized by the exchange bias induced at the interface between $Co_{90}Fe_{10}$ and $Mn_{80}Ir_{20}$. After the deposition, the GMR stacks were microfabricated into rectangular shapes of 30 μm × 300 μm by the lithography processes and Ar^+ ion milling. The Ar^+ ions with an incident energy of 700 eV were generated by a Kaufman-type ion source and were incident perpendicularly to the sample surface. After the milling, 250 nm-thick Al_2O_3 layer and 250 nm-thick metallic wire with the size of 60 μm × 300 μm were deposited on top of the structured GMR device by the lift-off technique. The Al_2O_3 layer acts as an insulator between the GMR device and the metallic wire through which the ac current flows to generate high frequency modulation fields. After the microfabrication processes, all the samples were annealed at 270 °C under a magnetic field of 230 mT to align the direction of magnetization in the pinned layer and the uniaxial anisotropy of free layer in each device. The field was applied along the short axis of the GMR elements during the annealing. Fig. 3 (b) and (c) show the schematic of the GMR device structure and the optical microscope image of the microfabricated device, respectively. As shown in the figures, the GMR device has a single metallic wire on top of the GMR element to generate the magnetic field, in contrast to the previous studies (e.g. Ref. [5]), where coils to apply the modulation field were wounded around sensing devices. Since the free layer thickness of the GMR element is 10 nm and the distance between the GMR and metallic wire is 250 nm, which are both much smaller than the width of metallic wire of 60 μm, the field generated from the wire is assumed to be uniform in the free layer. Because the metallic wire has a small inductance, the frequencies of modulation fields f_{mod} can be easily increased. H_{mod} applied to the GMR device is proportional to the amplitude of current flowing through the wire and the inverse of the wire width. Fig. 4 shows the external field dependence of the resistance of the GMR device measured after completing all microfabrication processes. The result indicates that the magnetization in the GMR free layer saturates at approximately ±1.0 mT. In Fig. 4, the geometry of the resistance curve is distorted from the rectangular geometry as in Fig. 1. This may be caused by complexed domain structures originating from a relative balance of demagnetization field and uniaxial anisotropic field introduced by induced anisotropy. The domain structures of the $Ni_{80}Fe_{20}$ free layer have been already observed through the Kerr microscope in our previous work [32].

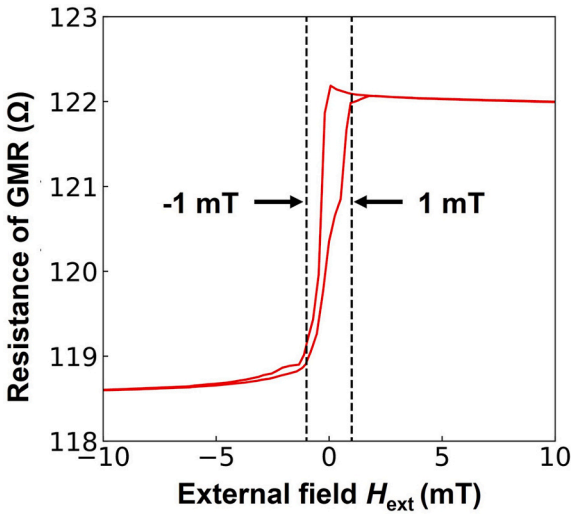


Fig. 4. Magnetic field vs. resistance of the GMR device measured after completing all microfabrication processes. Fields to saturate the magnetization of the free layer is estimated to be approximately ±1.0 mT as indicated by dashed lines.

2.3. Measurement setup

Fig. 5 shows a schematic of the measurement setup. The microfabricated GMR device was inserted into a bridge circuit. Here, a reference resistance device was inserted to compensate temperature drift in the bridge output caused by Joule heating of GMR devices, which originates from the dc bias voltage of the bridge circuit. Note that estimated current densities of the GMR devices are approximately 1 MA/cm^2. The reference resistance device exhibits a temperature coefficient nearly identical to that of the field-sensing GMR device. On the other hand, anisotropic magneto-resistance effect in the magnetic layer contributes to change the reference resistance, which is only 0.1 Ω and is negligible for that of the GMR device as in Fig. 4. The layer structure of the reference resistance device was SiO_2 substrate / Ta (5) / Cu (4) /$Ni_{80}Fe_{20}$ (10) / $Co_{90}Fe_{10}$ (3) / $Mn_{80}Ir_{20}$ (8) / Ta (2), where the deposition order of the NiFe free layer and the adjacent Cu layer was reversed to eliminate the GMR effect. The microfabrication process for the reference resistance device was identical to that used for the sensing GMR devices. The metallic wires of both the GMR and reference resistance were connected in series to a power amplifier (Kikusui, PBZ50) and a modulation current I_{mod} was directly supplied through the wires to

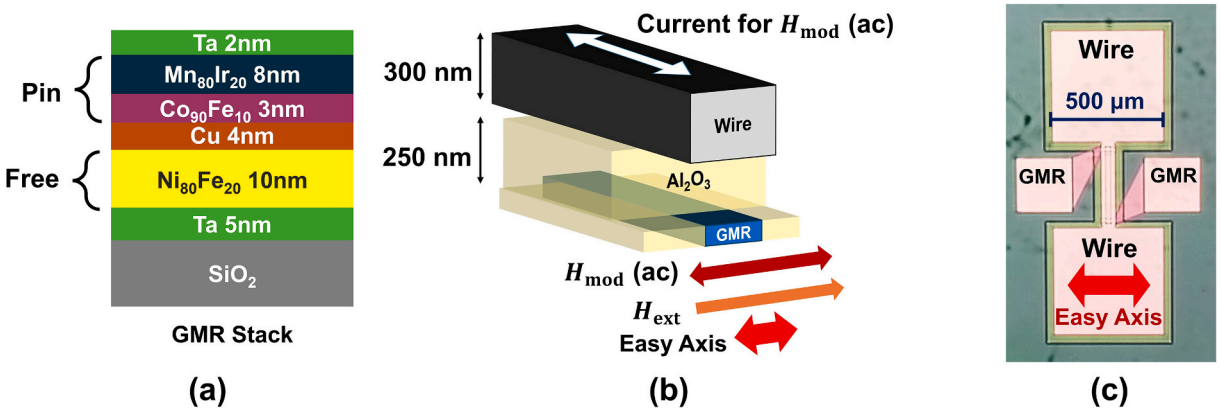


Fig. 3. (a) Illustration of the GMR stacks. The $Ni_{80}Fe_{20}$ and the $Co_{90}Fe_{10}$ layers are free and pinned layers, respectively. (b) Schematic of a GMR sensor device. The 300 nm-thick Al wire is placed above the GMR element, and the 250 nm-thick Al_2O_3 layer was inserted in between Al and GMR to insulate them. An ac current flowing through the Al wire produces H_{mod}, which oscillates the domain walls in the free layer. (c) Optical microscope image of the microfabricated device. The GMR element under the Al wire is not obvious, and the widths of GMR and Al are 30 μm and 60 μm, respectively.

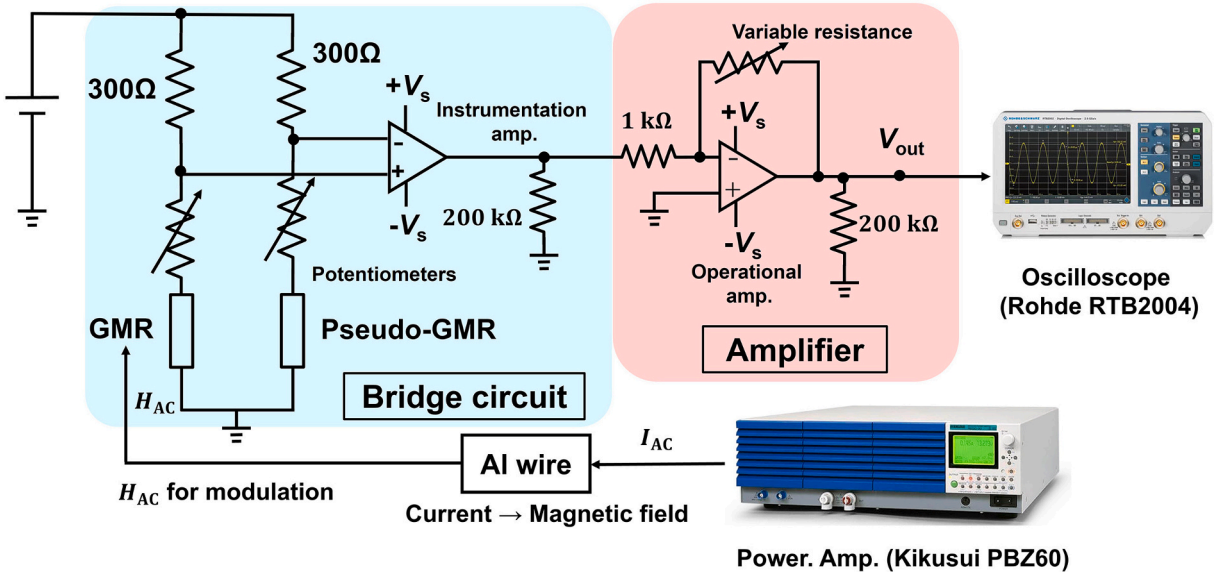


Fig. 5. Circuit diagram of the PWM-DWD sensor and its measurement setup. A GMR device and a reference resistance device are connected in the bridge circuit to compensate temperature drift due to Joule heating of the GMR device. The output of the bridge circuit was amplified by the instrumentation amplifier (IA) and operational amplifier (OA). The real time signal of the output was measured by the oscilloscope (Rhode & Schwarz, RTB2004). For noise spectrum measurements, an FFT analyzer (NI, PCI-4461) was used in place of the oscilloscope. The modulation current was supplied to both GMR and reference resistance by the power amplifier (Kikusui, PBZ60).

generate the modulation fields around the free layer of the GMR. The DC offset of the output was adjusted by tuning the potentiometers. The output of the bridge circuit was amplified by an instrumentation amplifier (IA) followed by an operation amplifier (OA). In the experiment, the gain of the IA was fixed at 84, whereas the gain of OA (G_{OA}) was varied between 10 and 100. The output signal of the circuit V_{out} was measured using an oscilloscope, and V_{ave} was estimated by numerical averaging of V_{out}.

The noise spectral density of the PWM-DWD sensors was measured using an FFT analyzer (National Instruments, PCI-4461). The sensor devices and the bridge circuits were placed inside a magnetic shield box with a shielding factor greater than 60 dB. The measurements were performed in the absence of an external field ($H_{ext} = 0$). The Hanning window function was used for the FFT analysis, and the signals were recorded for 1 s.

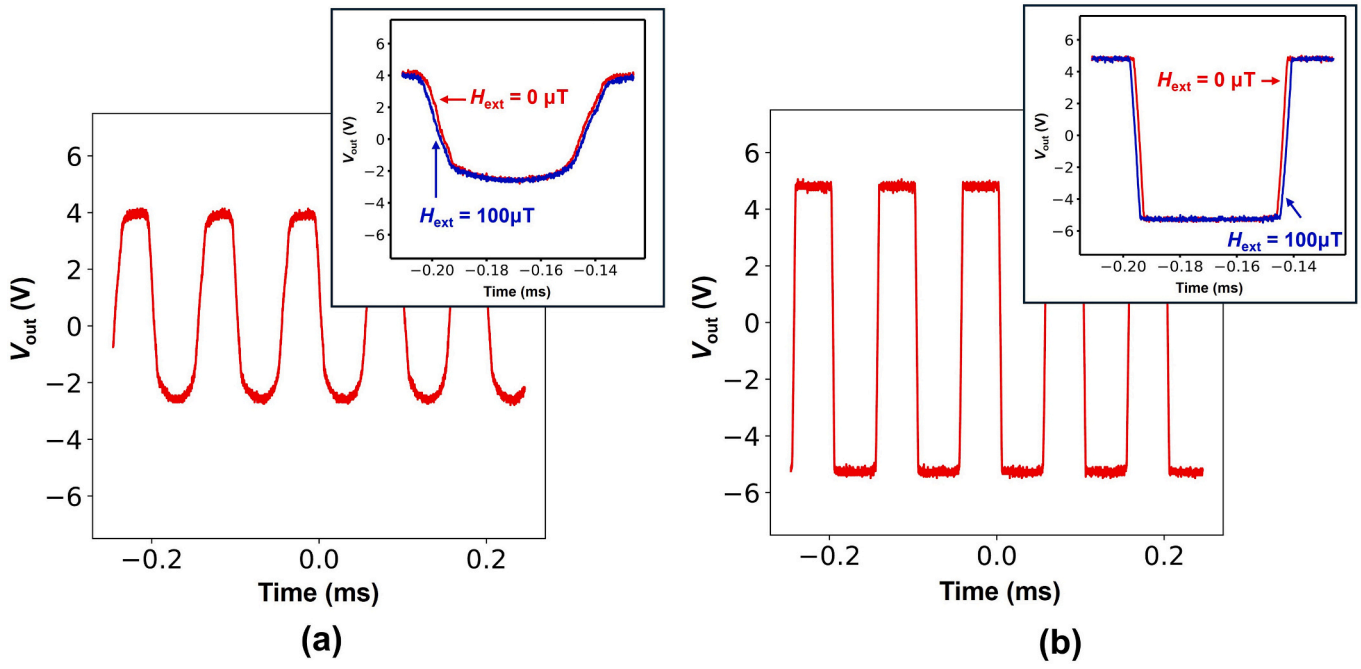


Fig. 6. V_{out} waveforms for (a) low OA gain ($G_{OA} = 10$) and (b) high OA gain ($G_{OA} = 100$) under the external field $H_{ext} = 0$. Insets in both figures show the one cycle waveform taken for $H_{ext} = 0$ (red curve) and 100 μT (blue curve). From the insets, duty ratio of the waveform varies depending on H_{ext}. For (a) low OA gain, the free layer of GMR was saturated by H_{mod}, and thus the shape of the waveform was not rectangle reflecting the distortion of MR loop. On the other hand, for (b) high OA gain, the V_{out} waveform became rectangle by driving OA into saturation, and the signal originating from the distortion of MR loop can be eliminated from V_{out}. (For interpretation of the references to colour in this figure legend, the reader is referred to the web version of this article.)

2.4. Operation check and waveform processing

Fig. 6 (a) shows the V_{out} waveform under the application of a modulation field with the amplitude H_{mod} of 1.4 mT and the frequency f_{mod} of 10 kHz. The red and the blue waveforms in the inset represent the data acquired when the external field $H_{ext} = 0$ and 100 μT, respectively. Note that G_{OA} was fixed at 10 and a supply voltage of OA was set to ±16 V to prevent voltage saturation in the OA. As shown in the inset, the duty ratio of the waveform varied with the application of H_{ext}, as described in the Sec. 2.1. Unlike in Fig. 1 (c), however, the V_{out} waveform did not exhibit a perfect rectangular shape; instead, the flat saturation regions between switching events appeared rounded. The rounded regions typically originate from the magnetization process of the GMR free layer as it approaches saturation, resulting in large output noise in the low frequency region. This will be discussed in Sec.4.1.

Therefore, we set G_{OA} to 100 and the OA supply voltage to ±6 V to intentionally saturate OA and produce square waveforms. By driving the OA into saturation, the rising and falling edges of the waveform become sharper, and the rounded regions of the waveform mentioned above were eliminated from V_{out}, which contribute to the reducing the magnetic noise. Hereafter, we refer to this method as the "saturation-mode". The V_{out} waveforms in Fig. 6 (b) were obtained by the saturation-mode. Similar to Fig. 6 (a), the inset in Fig. 6 (b) shows one cycle waveform measured at $H_{ext} = 0$ (red) and 100 μT (blue), respectively. The duty ratio changed in the same manner as in Fig. 6 (a), while the waveforms became more square-shaped, similar to those shown in Fig. 1 (c). Thus, we mainly discuss the results of the PWM-DWD modulation sensor operating in the saturation-mode in this paper unless otherwise stated.

3. Results and discussions 1: Output signals

3.1. Output signal (V) – External field (H) property

To discuss the sensor output in response to H_{ext}, V_{ave} was measured by sweeping H_{ext}. As described in Sec. 2.1, the sensor detects the magnetic fields through the duty ratio of the V_{out} waveform, which is reflected in its time-averaged value. Here, V_{ave} was obtained by numerically averaging V_{out} for 12 ms using the oscilloscope. Fig. 7 (a) shows the V_{ave}–H_{ext} characteristics measured under a modulation field with an amplitude H_{mod} of 1.4 mT and a frequency f_{mod} of 10 kHz. H_{ext} was swept between −100 μT to 100 μT. Note that an offset of V_{ave} is numerically removed.

As shown in Fig. 7 (a), the V_{ave}–H_{ext} curve clearly exhibited a linear relationship. To evaluate the linearity of the V_{ave}–H_{ext} characteristics, we used a parameter called "non-linearity" introduced in Ref. [31]. Non-linearity *NL* is defined as

$$NL = \frac{\max(\mathrm{data}(H_{ext}) - f(H_{ext}))}{\max f(H_{ext}) - \min f(H_{ext})}, \quad (2)$$

where data(H_{ext}) and f (H_{ext}) are the measured output data at H_{ext} and their linear fitting function, which can be written as a form of $aH_{ext} + b$, respectively. From Eq. (2), the *NL* in Fig. 7 (a) was calculated to be 1.99%.

To investigate the effect of the PWM-DWD technique, we compared the result in Fig. 7 (a) with the V_{ave}–H_{ext} curve of Fig. 7 (b), which was measured without applying a modulation field. As in Fig. 7 (a), H_{ext} was applied along the easy axis of the GMR free layer, and the offset component of V_{ave} was subtracted by a numerical calculation. The V_{ave}–H_{ext} curve exhibited distinct hysteresis, resembling a Rayleigh loop, which is typically observed in the magnetization curve of a ferromagnet within a narrow sweeping range. The *NL* value in this case was 10.58%, confirming that PWM-DWD technique is effective in reducing hysteresis and enhancing the linearity.

3.2. Modulation dependence in sensitivity

The sensitivity of the PWM-DWD sensor output, defined as the slope of V_{ave}–H_{ext} characteristics, was investigated by applying various H_{mod} and f_{mod}. In the experiment, f_{mod} was varied from 500 Hz to 100 kHz under nominal H_{mod} values of 1.1 mT, 1.4 mT and 1.7 mT, respectively, which were estimated based on the voltage applied to the wire generating the modulation field. The sensitivity was defined as the slope of the linear fitting function $f(H_{ext})$, which has already been introduced in the explanation of Eq. (2). Fig. 8 shows f_{mod} dependence of the sensor's sensitivity under different H_{mod} values. The sensitivity remained nearly constant over the investigated f_{mod} range, whereas it increased as H_{mod} decreased. One may note that the sensitivity slightly increased when f_{mod} exceeded 10 kHz under the same H_{mod}. This behavior was attributed to the impedance of the metallic wire on the GMR device and in the connecting cables used to supply current. In the experiment, H_{mod} is controlled by voltage applying to the current wire and the cables assuming their impedance remains constant. However, the impedance is supposed to increase when f_{mod} is 50 kHz and 100 kHz due to the parasitic inductance, resulting in the reduction of I_{mod}. Thus, the effective H_{mod} applied to the GMR device becomes smaller than the nominal value. The inset of Fig. 8 shows H_{mod} dependence of the sensitivity at $f_{mod} = 10$ kHz. It explains a clear proportionality to $1/H_{mod}$ as indicated by the red dotted approximation curve, which is in good agreement with Eq. (2). These results confirm that the sensitivity of the PWM-DWD sensor depends only on the amplitude of the modulation field and is essentially independent of the modulation frequency.

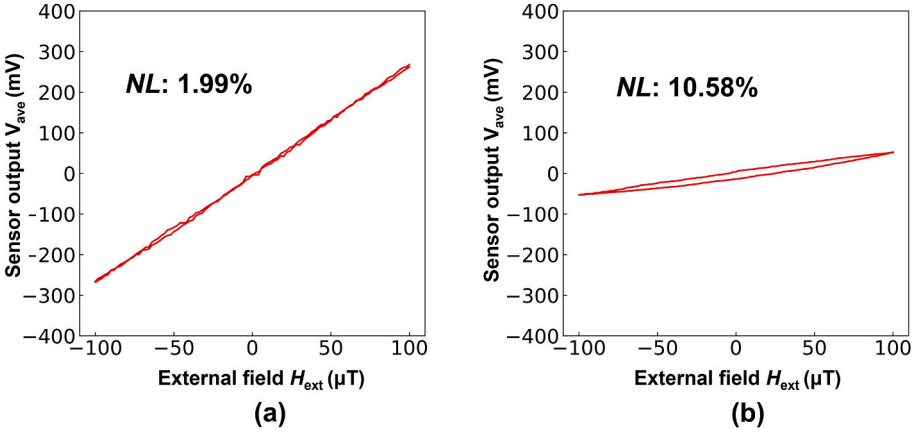


Fig. 7. V_{ave}–H_{ext} properties of the GMR sensors (a) with PWM-DWD modulation technique under the modulation field with the amplitude H_{mod} of 1.4 mT and the frequency f_{mod} of 10 kHz, and (b) without modulation field which was obtained in the same device.

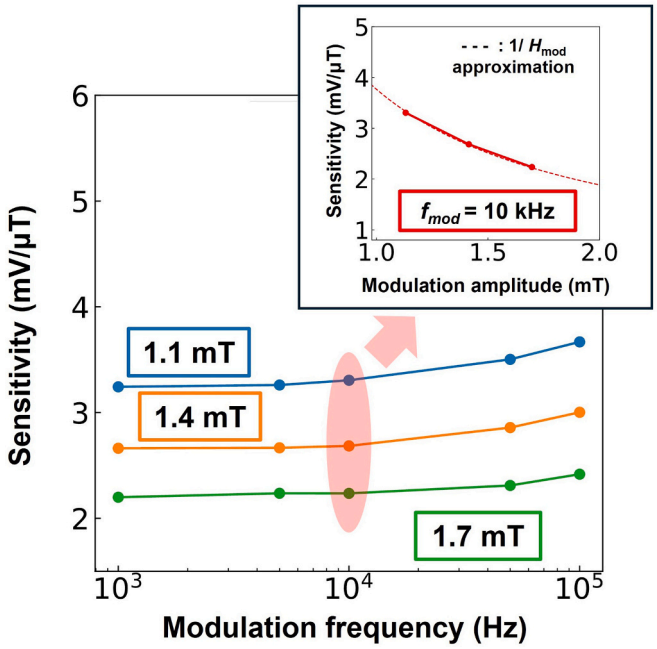


Fig. 8. f_{mod} dependence of sensitivity V_{ave}/H_{ext} under different H_{mod}. The sensitivity increased by reducing H_{mod}, while it was insensitive to f_{mod}. The inset shows the H_{mod} dependence of the sensitivity at f_{mod} of 10 kHz. A dotted curve indicates the $1/H_{mod}$ approximation of the obtained sensitivities. The approximation curve well explains the results and demonstrates the validity of Eq. (1).

3.3. Modulation dependence in linearity

The modulation frequency dependence of the non-linearity *NL* of the sensor output is plotted in Fig. 9. The red dashed line represents the non-linearity of the output signal measured without applying modulation to the same GMR sensor device. From the figure, the *NL* was significantly suppressed by applying the PWM-DWD technique, demonstrating the validity of the theory as described in Sec. 2.1. Furthermore, *NL* exhibited nearly constant values, independent of both H_{mod} and f_{mod}, indicating the modulation fields have no significant impact on *NL*. One may note that a slight increase in *NL* over 5% was observed when H_{mod} was 1.4 or 1.7 mT and f_{mod} was 100 kHz. This enhancement of *NL* is considered to be due to an increase in the noise of V_{out} (see Sec. 4.2 for details), rather than the hysteresis of the sensor output.

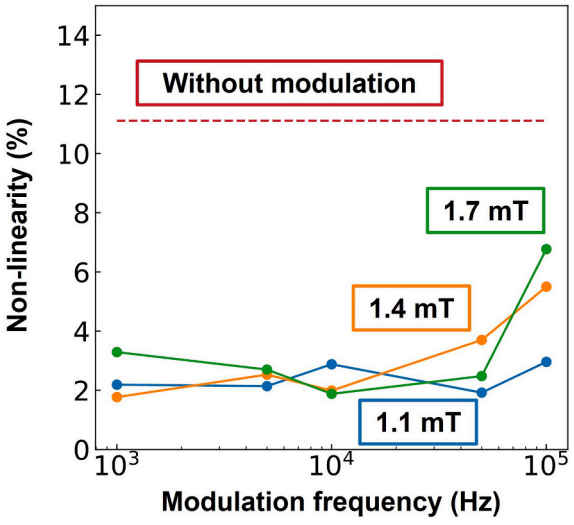


Fig. 9. f_{mod} dependence of non-linearity *NL* of the sensor output when various H_{mod} are applied to the GMR device. The red dashed line shows the results when no modulation fields are applied. *NL* of the sensor output decreased significantly by applying PWM-DWD technique. The greater nonlinearity was confirmed when f_{mod} of 100 kHz and H_{mod} of 1.4 or 1.7 mT, which results from the increase in the noise of the sensor output as in Fig. 11 (b).

4. Results and discussion 2: Noise analysis

4.1. Influence of saturation-mode in noise reduction

We first measured the circuit background noise by inserting 120 Ω metallic film resistors into the bridge circuit in place of the GMR and reference resistance devices. The metallic film resistors do not generate magnetic noise, and thus the sensor's circuit noise could be estimated. The magenta curve in Fig. 10 illustrates the result of the circuit noise measurement. In the figure, we confirmed $1/f$ noise in the low frequency region, which mainly originated from the IA and OA. Next, we inserted the GMR and reference resistance devices into the bridge circuit to measure the noise spectrum of V_{out} under a modulation field. To measure the noise spectrum under the condition shown in Fig. 6(a), where the operational amplifier was not saturated, G_{OA} and the OA supply voltage were set to 10 and ± 16 V, respectively. Here, we fixed H_{mod} at 1.1 mT and f_{mod} at 1 kHz. The black solid spectrum in Fig. 10 presents the measurement result, clearly indicating peaks corresponding to the modulation signal and its harmonics, with a significant enhancement of noise across the entire frequency range compared with the background noise. The large noise may have resulted from the rounded regions of V_{out}, which are discussed at the end of this section. Finally, we measured the noise spectrum of V_{out} when the saturation mode was applied. In this mode, G_{OA} was reset to 100, and the OA supply voltage was fixed at ±6 V as described in the Sec. 2.4. The blue curve in Fig. 10 shows the noise

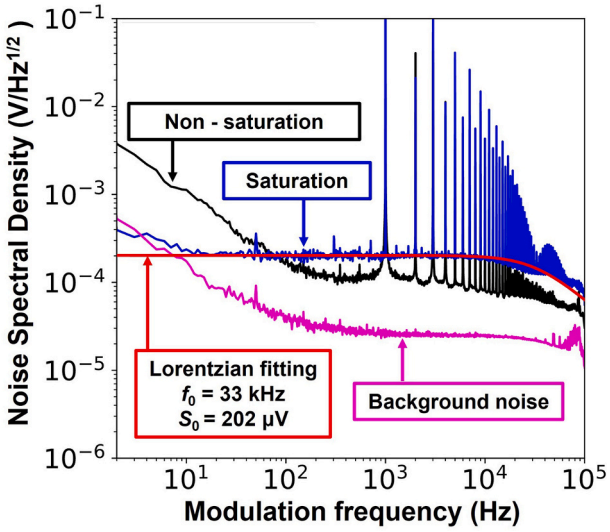


Fig. 10. Noise spectral density of V_{out} in the sensor operated under saturation (blue) and non-saturation (black) modes. The sensors were modulated under the conditions of H_{mod} = 1.1 mT and f_{mod} = 1 kHz. For comparison, background noise spectral density was shown as magenta line, where no modulation field was applied. The saturation-mode exhibited almost flat noise below f_{mod} and significantly reduced $1/f^n$ noise in the low frequency region compared to the non-saturation mode. Since the flat noise in blue spectrum is in good agreement with the Lorentzian fitting (red), we concluded the noise of saturation-mode mainly results from jitters originating from transitions in V_{out}. On the other hand, a slight noise increase apart from the flat noise was confirmed under 10 Hz even in the saturation-mode. This is due to the background $1/f$ noise, which contains both circuit noise and inherent magnetic noise in GMR devices. (For interpretation of the references to colour in this figure legend, the reader is referred to the web version of this article.)

spectrum of the sensor operating in the saturation mode. Obviously, the spectrum exhibited a flat noise, and the 1/f noise observed in the black curve was significantly reduced. The flat noise in the saturation mode originated from random telegraph noise (RTN) caused by fluctuations in the duty ratio, i.e. jitter, of the modulated waveform shown in Fig. 6 (b). In general, RTN follows a Lorentzian distribution characterized by a flat region at low frequencies that rolls off beyond a certain frequency [35]. The noise spectral density of RTN, V_N can be expressed as follows:

$$V_N(f) = \sqrt{\frac{V_0^2}{1+\left(\frac{f}{f_0}\right)^2}}, \tag{3}$$

where V_0 and f_0 stand for the noise voltage at DC component and a roll-off frequency, respectively. The red curve in Fig. 10 corresponds to a fitted result for the blue curve. The red curve shows good agreement with the blue spectrum across all frequencies except at the modulation signal and its harmonics, and V_0 and f_0 were determined to be 202 μV and 33 kHz, respectively. The 1/f noise in the saturation mode was significantly smaller than that of black curve in Fig. 10, which was obtained when OA saturation was avoided. This indicates that the large 1/f noise observed in the black curve originates from the rounded regions between switching events of V_{out} in Fig. 6 (a), where the free layer magnetization was nearly saturated, as mentioned in Sec. 2.4. We presume that the rounded regions of V_{out} in Fig. 6 (a) are associated with inhomogeneous nucleation and expansion of magnetic domains in the free layer near saturation. Thermal fluctuations of these domains are considered to contribute to the observed $1/f^n$ noise in the non-saturation mode. On the other hand, driving the OA in the saturation mode eliminates these rounded regions in V_{out}, and thus the saturation mode effectively reduces low frequency noise in the PWM-DWD sensor.

4.2. Modulation dependence of noise properties

The noise spectral densities of the PWM-DWD sensor operated at various modulation frequencies— f_{mod} = 500 Hz, 1 kHz, and 10 kHz—are shown in Fig. 11 (a). Here, the modulation field was fixed at H_{mod} = 1.1 mT. As shown in the figure, the flat noise level decreased, and the roll-off frequency increased with increasing f_{mod}. This indicates that the RTN observed in the PWM-DWD sensor operating in the saturation mode was suppressed as f_{mod} increased. Fig. 11 (b) shows the 120 Hz components of the noise spectral density (NSD) plotted as a function of f_{mod}. Here, we compared two cases with the modulation fields of H_{mod} = 1.1 and 1.7 mT. When jitters in the modulation waveform are proportional to the modulation field's period, the flat noise level originating from RTN becomes proportional to $1/f_{mod}^{1/2}$. Therefore, we fitted the data using $1/f_{mod}^{1/2}$ approximation for f_{mod} below 10 kHz. The dashed lines represent the $1/f_{mod}^{1/2}$ approximation, which agrees well with the experimental NSDs at 120 Hz for both H_{mod} values. However, a significant increase of NSD beyond 50 kHz was confirmed when H_{mod} is 1.7 mT. To investigate the origin of this increased noise, we observed the falling transitions of V_{out} waveforms under each modulation condition. Fig. 12 (a) shows V_{out} measured under the condition of H_{mod} = 1.1 mT and f_{mod} = 1 kHz. Here, the horizontal axis is normalized by the modulation period T_{mod}, which is 1 ms under this condition. The figure presents the waveforms superimposed over 3 cycles, intentionally selected to highlight the largest jitter variations for clarity. The measurement revealed that the transitions were completed within 0.03 t/T_{mod} following random trajectories, indicating the stochastic nature of domain wall displacement. Meanwhile, Fig. 12 (b) shows V_{out} waveforms recorded when f_{mod} was increased to 100 kHz. This result suggests that the increase of f_{mod} is effective in suppressing the stochastic trajectories of the V_{out} waveform owing to smoother domain wall propagation in the free layer, thereby reducing RTN. Fig. 12 (c) shows the modulation waveform recorded when H_{mod} increased to 1.7 mT under f_{mod} of 100 kHz. The inset presents an enlarged view of the waveform between t/T_{mod} of 0.44 and 0.47. As in Fig. 12 (c), each falling transition exhibited an almost identical shape, though they are slightly shifted relative to one another. These phenomena can be interpreted as follows. In the case of H_{mod} = 1.1 mT, the modulation field did not fully saturate the free layer; thus, the magnetization reversal was primarily dominated by domain expansion. In contrast, at the higher H_{mod} of 1.7 mT, domain nucleation also contributed significantly to the magnetization reversal process in addition to the domain expansion, and the stochastic nature of this domain nucleation further increased NSD as in Fig. 11 (b). From these results, we conclude that optimal combinations of f_{mod} and H_{mod} to minimize the noise floor of PWM-DWD sensors, since different noise sources dominate under different modulation conditions. Further investigation into the relationship between the sensor noise and the magnetization process of the free layer is required to elucidate the underlying physical origin of these noise sources.

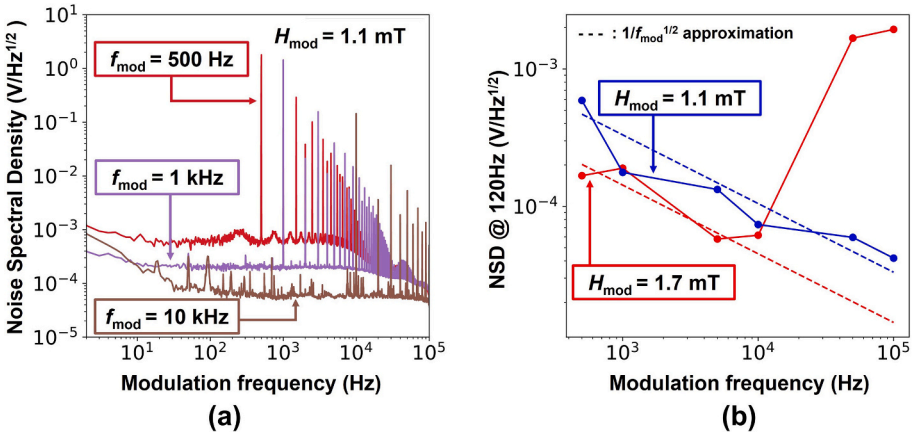


Fig. 11. (a) Noise spectral density of the PWM-DWD sensor operated under H_{mod} = 1.1 mT and f_{mod} = 500 Hz, 1 kHz, and 10 kHz. The flat noise spectral density in the frequency of 100 Hz–10 kHz reduced as f_{mod} increases. (b) The noise spectrum densities at 120 Hz are plotted as a function of f_{mod}, where H_{mod} was set at 1.1 mT (blue circles) and 1.7 mT (red circles). The dashed lines indicate the $1/f_{mod}^{1/2}$ approximation fitted to the data. Since the $1/f_{mod}^{1/2}$ approximation well explains the results below 10 kHz, the jitters, i.e., the source of random telegraph noise, are proportional to the sweep rate of the modulation field. However, significant increase of the noise was confirmed above 50 kHz when H_{mod} was 1.7 mT. We consider a different stochastic mechanism, such as domain nucleation, dominates the noise when the PWM-DWD sensor operated under high H_{mod} and high f_{mod}. (For interpretation of the references to colour in this figure legend, the reader is referred to the web version of this article.)

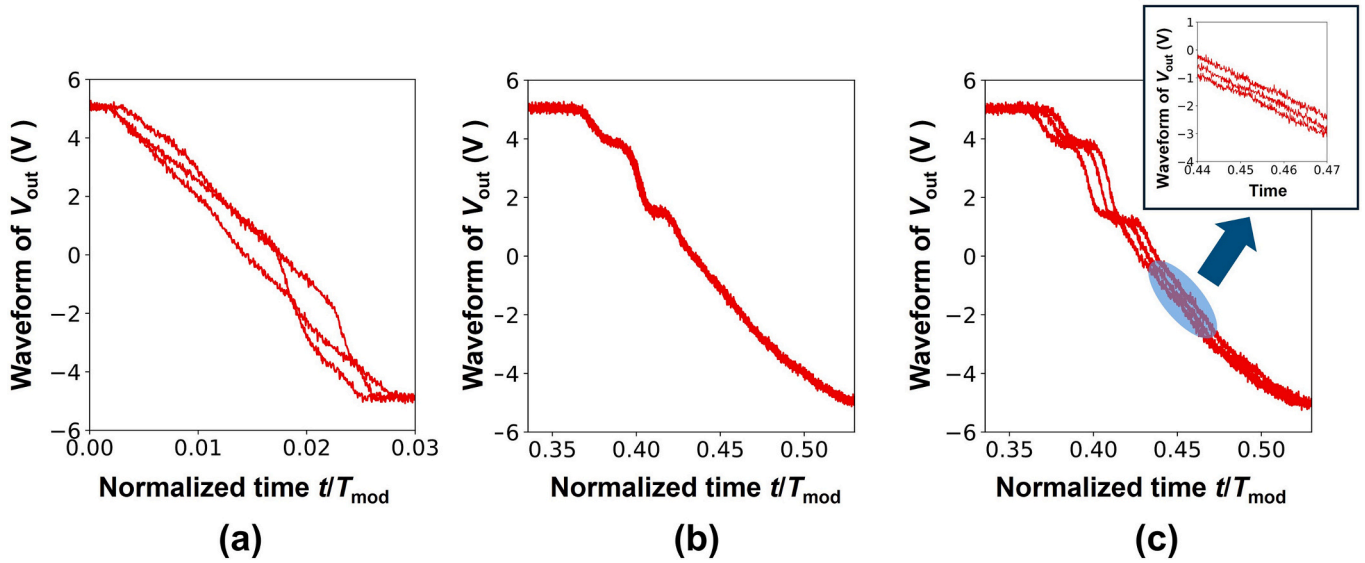


Fig. 12. Falling transitions of V_{out} waveforms under the modulation conditions of (a) H_{mod} = 1.1 mT and f_{mod} = 1 kHz, (b) H_{mod} = 1.1 mT and f_{mod} = 100 kHz, and (c) H_{mod} = 1.7 mT and f_{mod} = 100 kHz. Horizontal axis is normalized by the modulation period, T_{mod}. The figures show the waveforms superimposed over 3 cycles. Note that inset in (c) show the enlarged view in the range of t/T_{mod} = 0.44–0.47. In Fig. (a), the three transitions followed random trajectories, which suggests stochastic domain wall displacement. In Fig. (b) and (c), on the other hand, each falling transition has an almost identical shape, implying smooth wall propagation. However, the falling transitions in Fig. (c) shifted against each other. We consider this phenomenon contributes to the increased NSD as shown in Fig. 11 (b).

4.3. Material dependence

To reduce the sensor's noise through material optimization of the free layer, we prepared several GMR sensors with different free layer materials and compared their noise spectral densities. Here, we used $Co_{20}Fe_{60}B_{20}$ and $(Co_{90}Fe_{10})_{92}B_8$ instead of NiFe to introduce variations in coercivity of the free layers. Fig. 13 (a) shows magnetization curves of NiFe, $Co_{20}Fe_{60}B_{20}$, and $(Co_{90}Fe_{10})_{92}B_8$ single layers measured using a vibrating sample magnetometer (VSM). From the results, NiFe, $Co_{20}Fe_{60}B_{20}$ and $(Co_{90}Fe_{10})_{92}B_8$ were confirmed to exhibit coercivities of 0.13 mT, 0.3 mT and 0.42 mT, respectively. Fig. 13 (b) shows the noise spectra of PWM-DWD sensors with different free layer materials, measured under conditions of H_{mod} = 1.1 mT and f_{mod} = 10 kHz. The sensors with free layers made of higher coercivity material clearly exhibited grater noise levels in the low frequency region. Fig. 13 (c) shows the dependence of NSD at 120 Hz on the free layer coercivity, extracted from the noise spectra measured under H_{mod} = 1.1 mT while f_{mod} varying from 1 kHz to 100 kHz. Smaller NSDs at 120 Hz were observed for sensors operated at higher modulation frequency and with free layers of lower coercivity. Therefore, we conclude that low coercivity materials are preferable for reducing the noise level of PWM-DWD sensors.

To identify the reason of increase in the noise of the GMR sensors having free layers with high coercivity, we re-examined the falling transitions in the V_{out} waveforms. Fig. 14 (a), (b) and (c) show the comparisons of falling trajectories for GMR devices employing NiFe, $Co_{20}Fe_{60}B_{20}$, and $(Co_{90}Fe_{10})_{92}B_8$ free layers, respectively. Unlike the sensor with NiFe free layer, the other two GMR sensors exhibited falls with random slopes, and the randomness appears to be increased with increasing coercivity of the free layer. This randomness results in a higher noise level with a $1/f^n$ -type spectrum in the low-frequency region, particularly for the device with $(Co_{90}Fe_{10})_{92}B_8$ free layer. We

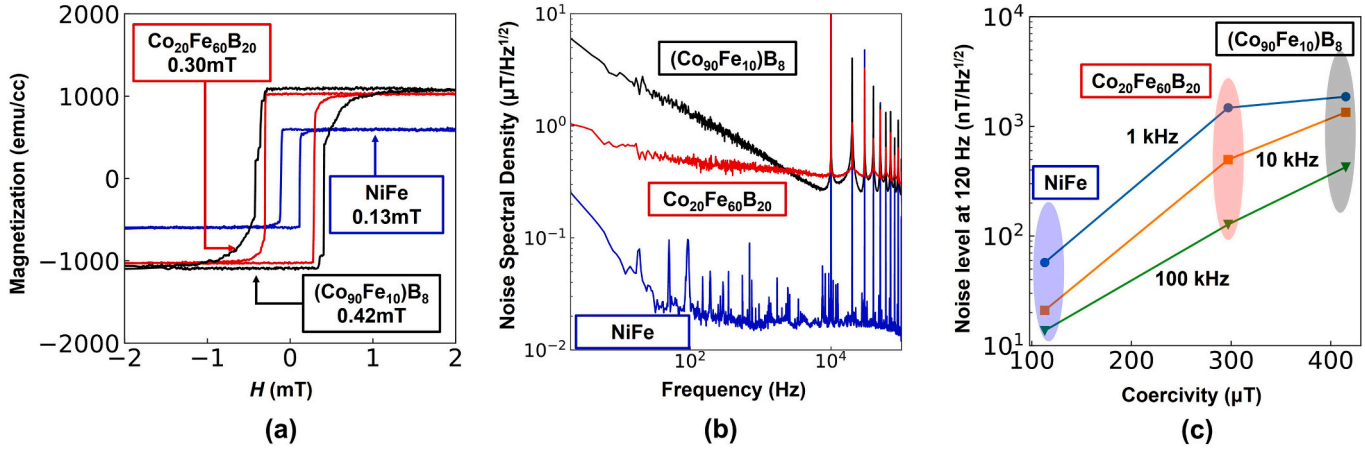


Fig. 13. (a) Magnetization curves of NiFe, $Co_{20}Fe_{60}B_{20}$ and $Co_{83}Fe_9B_8$ single layers. Coercivities of each material were 0.13 mT, 0.30 mT and 0.42 mT, respectively. (b) Input referred noise spectral density of PWM-DWD sensors having the three different free layer materials. The spectra were measured under H_{mod} of 1.1 mT and f_{mod} of 10 kHz. (c) Free layer coercivity dependence of NSD at 120 Hz extracted from the noise spectra measured under the condition that H_{mod} = 1.1 mT and f_{mod} was varied as 1 kHz, 10 kHz, and 100 kHz. Smaller input referred noise were observed for the sensors operated under higher f_{mod} and with free layers exhibiting smaller coercivity.

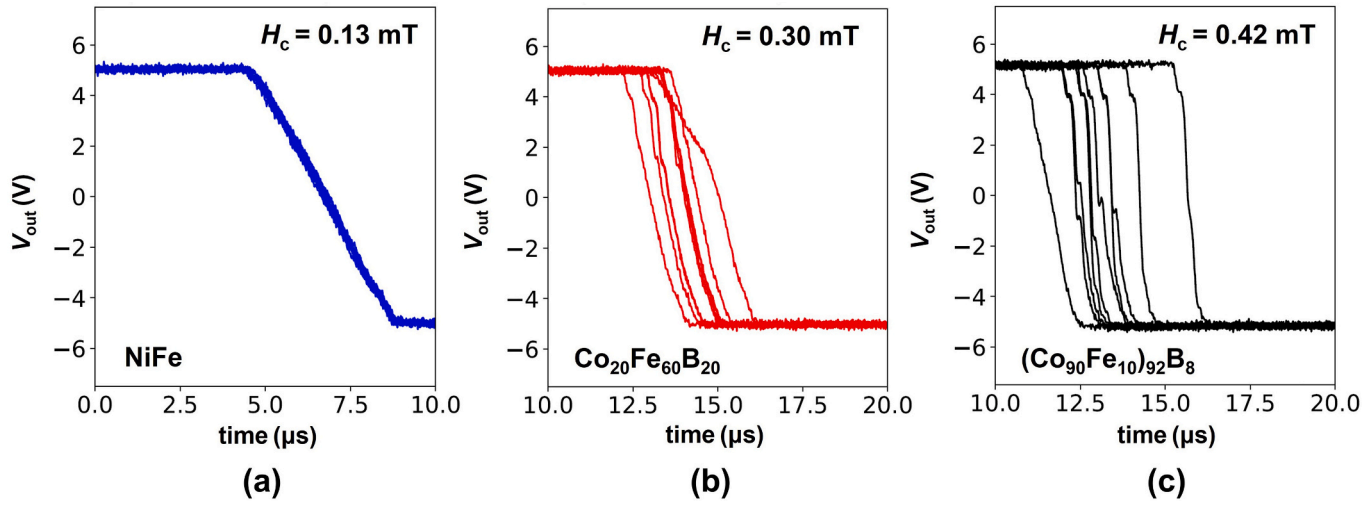


Fig. 14. (a) Falling transitions of V_{out} in GMR sensors with (a) NiFe, (b) $Co_{20}Fe_{60}B_{20}$ and (c) $Co_{83}Fe_9B_8$ single layers, respectively. Note that H_{mod} was 1.1 mT and f_{mod} was 10 kHz. Randomness in trajectories increased as coercivity increased. We consider the increase in coercivity causes stochastic variations in both domain wall nucleation and velocity.

attribute the increased noise in the sensors with $Co_{20}Fe_{60}B_{20}$ and $(Co_{90}Fe_{10})_{92}B_8$ free layers to random variations in both domain wall nucleation and velocity. Indeed, several works have reported the velocities of domain walls is determined by heights of energy barriers of pinning sites, which are closely related to coercivity [36,37]. Since these energy barriers fluctuate stochastically due to thermal fluctuations in the system, velocity of domain walls is also considered to exhibit stochastic behavior. However, further investigation is required for a more detailed understanding.

4.4. Minimum detectivity and outlook

Next, we investigated the minimum detectivity of the present PWM-DWD sensors. In the previous sections, a low NSD was obtained using a GMR sensor with a NiFe free layer, operated under the conditions of f_{mod} = 100 kHz and H_{mod} = 1.1 mT. Here, the external field of H_{ext} = 140 nT_{rms} at 120 Hz was applied as a reference signal. Due to the restriction of the experimental setup, H_{ext} was applied by the current flowing through the metallic wire above the GMR element in addition to the current used to generate H_{mod}. The blue spectrum in Fig. 15 shows the measurement result. As shown in the figure, the H_{ext} signal at 120 Hz was clearly confirmed, and the field detectivity was estimated to be approximately 14 nT from the NSD at 120 Hz. The NSD of the PWM-DWD sensor output was nearly identical to the circuit background noise shown by the magenta line in the figure. This indicates that the RTN originating from the stochastic nature of DWD (see Fig. 11 (a)) is suppressed below the circuit noise level by operating the sensor at a high modulation frequency of 100 kHz. However, the noise of the PWM-DWD sensor was approximately 100 times larger than that of our previous DWD sensor, which was 300 $pT/Hz^{1/2}$ at 10 Hz. To further reduce the noise and improve field detectivity, both minimizing the sensor circuit noise and optimizing the free layer materials in the GMR device are necessary. For example, G_{OA} was set to 100 in this experiment to drive the sensor in the saturation-mode. However, a larger G_{OA} amplifies the circuit background noise, leading to a lower SNR in the sensor output. Therefore, the value of G_{OA} should be minimized while ensuring that the V_{out} waveform remains saturated by the OA. Enhancing magnetoresistance ratio of the GMR device is effective for operating the sensor in the saturation mode even with a smaller G_{OA}. Moreover, materials with low coercivity, such as CoFeSiB free layer [38], are promising candidates for the free layer in GMR device. This is because low coercivity free layers in PWM-DWD sensors can operate under small H_{mod}, contributing to increased sensitivity and reduced noise, as discussed in Sec. 3.2. Further

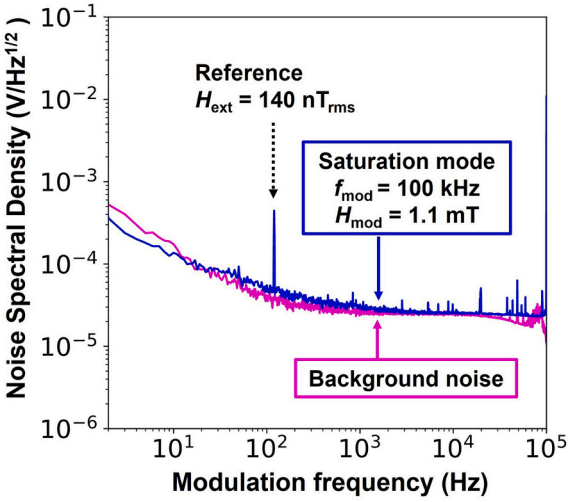


Fig. 15. Noise spectral density of PWM-DWD sensor with NiFe free layer operated under the conditions of H_{mod} = 1.1 mT and f_{mod} = 100 kHz. Here, an external field H_{ext} of 140 nT at a frequency of 120 Hz is applied as a reference signal. The circuit background noise is shown by magenta line in the figure. The detectivity of the present PWM-DWD sensor is estimated to be 14 $nT/Hz^{1/2}$. The sensor's noise spectrum exhibited almost identical to the background noise of the circuit, suggesting RTN originating from the stochastic nature of domain wall displacement of the free layers is suppressed below the circuit noise level in this modulation condition. (For interpretation of the references to colour in this figure legend, the reader is referred to the web version of this article.)

increasing f_{mod}, e.g., 1–10 MHz, is also expected to be effective in reducing RTN.

5. Conclusion

In this paper, we investigated the fundamental properties of PWM-type GMR sensors utilizing DWD technique. In PWM-DWD sensors, large, high-frequency modulation fields were applied along the easy axis of GMR devices, and the magnetization in the free layers was periodically saturated. By driving the operational amplifier in the sensor circuit in the saturation mode, the output waveform of the GMR device became square-shaped, and the duty ratio of the square wave depended on the external magnetic field. The sensor output in the saturation mode

exhibited small nonlinearity of approximately 2%, regardless of the amplitude and frequency of the modulation field. The sensitivity of the sensor was found to be inversely proportional to the modulation field, $1/H_{mod}$, and was not affected by the modulation frequency. The sensor operated in the saturation mode exhibited a flat noise spectrum in the low-frequency region, originating from the random telegraph noise (RTN). The RTN decreased with increasing the modulation frequency f_{mod}, exhibiting below the sensor circuit noise level when the modulation field was 1.1 mT at 100 kHz. The origin of the RTN is attributed to the stochastic nature of the domain wall propagation, and both increasing the modulation frequency and reducing the coercivity of the free layer are expected to be effective in suppressing RTN. In this study, we achieved the minimum detectivity of 14 nT/Hz$^{1/2}$ at 120 Hz by operating the sensor under conditions of $H_{mod} = 1.1$ mT and $f_{mod} = 100$ kHz. For further improvement of sensor's detectivity, minimizing the gain of the operational amplifier within a range that maintains the saturation of the V_{out} waveform is expected to be effective. Moreover, fabricating GMR devices with larger magnetoresistance ratios and lower coercivity could further enhance detectivity. In conclusion, the proposed PWM-DWD sensor represents one of the promising candidates for real-time detection of bio-magnetic fields, such as in magnetocardiography and magnetoencephalography applications.

CRediT authorship contribution statement

Kosuke Komuro: Writing – review & editing, Writing – original draft, Visualization, Validation, Software, Resources, Project administration, Methodology, Investigation, Formal analysis, Data curation, Conceptualization. **Arata Kawamura:** Software, Resources. **Hirofumi Suto:** Writing – review & editing, Supervision, Software, Resources. **Tomoya Nakatani:** Writing – review & editing, Supervision, Resources, Project administration, Methodology. **Daiki Oshima:** Supervision, Conceptualization. **Takeshi Kato:** Writing – review & editing, Supervision, Project administration, Funding acquisition, Conceptualization.

Declaration of Competing Interest

The authors declare the following financial interests/personal relationships which may be considered as potential competing interests: [Takeshi Kato reports financial support was provided by Japan Science and Technology Agency. Takeshi Kato reports financial support was provided by Government of Japan Ministry of Education Culture Sports Science and Technology. Takeshi Kato reports financial support was provided by Nagoya University. If there are other authors, they declare that they have no known competing financial interests or personal relationships that could have appeared to influence the work reported in this paper.].

Acknowledgments

This work was supported in part by JST A-STEP Grant Number JPMJTR24R7, Japan. This work was also supported in part by the Research Program “Dynamic Alliance for Open Innovation Bridging Human, Environment and Materials” in “Network Joint Research Center for Materials and Devices”. A part of this work was performed under the Project of Creation of Life Innovation Materials for Interdisciplinary and International Researcher Development of the Ministry of Education, Culture, Sports, Science and Technology (MEXT), Japan. A part of this work was conducted at the Next-generation biomaterials Hub, Nagoya University, JPMXP1224NU5222, supported by Advanced Research Infrastructure for Materials and Nanotechnology in Japan of MEXT, Japan.

Data availability

Data will be made available on request.

References

[1] G.L. Pearson, A magnetic field strength meter employing the hall effect in Germanium, Rev. Sci. Instrum. 19 (4) (1948) 263–265, https://doi.org/10.1063/1.1741240.
[2] Z. Zhou, et al., Advancements in research and current applications of ‘quantum sensor: superconducting quantum interference device, Euro. Phys. J. Special Topics (2025), https://doi.org/10.1140/epjs/s11734-025-01492-4.
[3] V. Pizzella, S. Della Penna, C. Del Gratta, G.L. Romani, SQUID systems for biomagnetic imaging, Supercond. Sci. Technol. 14 (7) (2001) R79–R114, https://doi.org/10.1088/0953-2048/14/7/201.
[4] P. Ripka, Review of fluxgate sensors, Sensors Actuators A Phys. 33 (3) (1992) 129–141, https://doi.org/10.1016/0924-4247(92)80159-z.
[5] C. Lei, X.-C. Sun, Y. Zhou, Noise analysis and improvement of a micro-electro-mechanical-systems fluxgate sensor, Measurement 122 (2018) 1–5, https://doi.org/10.1016/j.measurement.2018.03.007.
[6] R. Bazinet, A. Jacas, G.A.B. Confalonieri, M. Vazquez, A Low-Noise Fundamental-Mode orthogonal fluxgate magnetometer, IEEE Trans. Magn. 50 (5) (2014) 1–3, https://doi.org/10.1109/tmag.2013.2292834.
[7] K. Mohri, T. Kohsawa, K. Kawashima, H. Yoshida, L.V. Panina, Magneto-inductive effect (MI effect) in amorphous wires, IEEE Trans. Magn. 28 (5) (1992) 3150–3152, https://doi.org/10.1109/20.179741.
[8] T. Uchiyama, K. Mohri, Y. Honkura, L.V. Panina, Recent advances of Pico-Tesla Resolution Magneto-Impedance Sensor based on Amorphous Wire CMOS IC MI sensor, IEEE Trans. Magn. 48 (11) (2012) 3833–3839, https://doi.org/10.1109/tmag.2012.2198627.
[9] R. Rottmayer, N.J.-G. Zhu, A new design for an ultra-high density magnetic recording head using a GMR sensor in the CPP mode, IEEE Trans. Magn. 31 (6) (1995) 2597–2599, https://doi.org/10.1109/20.490065.
[10] N.S. Mao, et al., Commercial TMR heads for hard disk drives: characterization and extendibility at 300 gbit2, IEEE Trans. Magn. 42 (2) (2006) 97–102, https://doi.org/10.1109/tmag.2005.861788.
[11] H.A.M. Van Den Berg, et al., GMR angle detector with an artificial antiferromagnetic subsystem (AAF), J. Magn. Magn. Mater. 165 (1–3) (1997) 524–528, https://doi.org/10.1016/s0304-8853(96)00607-5.
[12] C. Giebeler, D.J. Adelerhof, A.E.T. Kuiper, J.B.A. Van Zon, D. Oelgeschläger, G. Schulz, Robust GMR sensors for angle detection and rotation speed sensing, Sens. Actuators A Phys. 91 (1–2) (2001) 16–20, https://doi.org/10.1016/s0924-4247(01)00510-6.
[13] S. Wang, D. Peng, Z. Wu, Embedded position detection for permanent magnet synchronous motor with Built-In magnets, IEEE Sensors J. 19 (21) (2019) 9818–9825, https://doi.org/10.1109/jsen.2019.2928336.
[14] A. Patel, M. Ferdowsi, Current Sensing for Automotive Electronics—A survey, IEEE Trans. Vehicular Technol. 58 (8) (2009) 4108–4119, https://doi.org/10.1109/tvt.2009.2022081.
[15] T.J. Brauhn, M. Sheng, B.A. Dow, H. Nogawa, R.D. Lorenz, Module-Integrated GMR-Based current sensing for Closed-Loop control of a motor drive, IEEE Trans. Ind. Appl. 53 (1) (2016) 222–231, https://doi.org/10.1109/tia.2016.2614771.
[16] S. Mostufa, et al., Giant magnetoresistance based biosensors for cancer screening and detection, ACS Appl. Bio Mater. 6 (10) (2023) 4042–4059, https://doi.org/10.1021/acsabm.3c00592.
[17] T. Klein, et al., Development of a multiplexed giant magnetoresistive biosensor array prototype to quantify ovarian cancer biomarkers, Biosens. Bioelectron. 126 (2018) 301–307, https://doi.org/10.1016/j.bios.2018.10.046.
[18] S. Mostufa, P. Yari, B. Rezaei, K. Xu, K. Wu, Flexible Magnetic Field nanosensors for Wearable Electronics: a review, ACS Appl. Nano Mater. 6 (15) (2023) 13732–13765, https://doi.org/10.1021/acsanm.3c01936.
[19] D. Su, et al., Ultra-flexible giant magnetoresistance biosensors for lab-on-a-needle biosensing, Adv. Mater. Interfaces 10 (7) (2023), https://doi.org/10.1002/admi.202201417.
[20] S. Mostufa, S. Liang, V.K. Chugh, J.-P. Wang, K. Wu, Spintronic devices for biomedical applications, Npj Spintronics 2 (1) (2024), https://doi.org/10.1038/s44306-024-00031-6.
[21] B. Lim, et al., Advances and key technologies in magnetoresistive sensors with high thermal stabilities and low field detectivities, APL Mater. 10 (5) (2022), https://doi.org/10.1063/5.0087311.
[22] K. Fujiwara, et al., Magnetocardiography and magnetoencephalography measurements at room temperature using tunnel magneto-resistance sensors, Appl. Phys. Express 11 (2) (2018) 023001, https://doi.org/10.7567/apex.11.023001.
[23] A. Kanno, et al., Scalp attached tangential magnetoencephalography using tunnel magneto-resistive sensors, Sci. Rep. 12 (1) (2022), https://doi.org/10.1038/s41598-022-10,155-6.
[24] A. Guedes, J.M. Almeida, S. Cardoso, R. Ferreira, P.P. Freitas, Improving magnetic field detection limits of spin valve sensors using magnetic flux guide concentrators, IEEE Trans. Magn. 43 (6) (2007) 2376–2378, https://doi.org/10.1109/tmag.2007.893119.
[25] S. Manceau, et al., Large amplification of the sensitivity of symmetric-response magnetic tunnel junctions with a high gain flux concentrator, Appl. Phys. Lett. 123 (8) (2023), https://doi.org/10.1063/5.0160544.
[26] M. Oogane, et al., Sub-pT magnetic field detection by tunnel magneto-resistive sensors, Appl. Phys. Express 14 (12) (2021) 123002, https://doi.org/10.35848/1882-0786/ac3809.
[27] T. Tatsuoka, et al., Measurement of somatosensory evoked magnetic fields using an adjustable magnetoresistive sensor array, Sens. Actuators A Phys. 374 (2024) 115456, https://doi.org/10.1016/j.sna.2024.115456.

[28] G.A. Wang, S. Nakashima, S. Arai, T. Kato, S. Iwata, High sensitivity giant magnetoresistance magnetic sensor using oscillatory domain wall displacement, J. Appl. Phys. 107 (9) (2010), https://doi.org/10.1063/1.3360585.
[29] G.A. Wang, Y. Masuda, T. Kato, S. Iwata, Influence of the free-layer domain structure on domain-wall displacing type field sensors, J. Appl. Phys. 109 (7) (2011), https://doi.org/10.1063/1.3561810.
[30] G.A. Wang, S. Arai, T. Kato, S. Iwata, Low-drift giant magnetoresistive field sensor using modulation of free-layer magnetization direction, J. Phys. D. Appl. Phys. 44 (23) (2011) 235003, https://doi.org/10.1088/0022-3727/44/23/235003.
[31] K. Komuro, D. Oshima, T. Kato, Fabrication of GMR sensors with antiphase magnetization modulation and Closed-Loop operation, IEEE Trans. Magn. 59 (11) (2023) 1–5, https://doi.org/10.1109/tmag.2023.3284398.
[32] K. Komuro, D. Oshima, T. Kato, Domain Wall Displacement Modulation GMR Sensors with Closed-Loop Current-Field Feedback, J. Magnetics Soc. Japan 48 (2) (2024) 34–39, https://doi.org/10.3379/msjmag.2403r004.
[33] P.D. Dimitropoulos, J.N. Avaritsiotis, E. Hristoforou, A novel micro-Fluxgate sensor based on the AMR effect of ferromagnetic film-resistors, Sensors Actuators A Phys. 107 (3) (2003) 238–247, https://doi.org/10.1016/s0924-4247(03)00378-9.
[34] L. Breth, T. Dimopoulos, J. Schotter, K. Rott, H. Bruckl, D. Suess, Fluxgate principle applied to a magnetic tunnel junction for weak magnetic field sensing, IEEE Trans. Magn. 47 (6) (2011) 1549–1553, https://doi.org/10.1109/tmag.2011.2106114.
[35] H. Xi, J. Loven, R. Netzer, J.I. Guzman, S. Franzen, S. Mao, Thermal fluctuation of magnetization and random telegraph noise in magnetoresistive nanostructures, J. Phys. D. Appl. Phys. 39 (10) (2006) 2024–2029, https://doi.org/10.1088/0022-3727/39/10/007.
[36] P. Chauve, T. Giamarchi, P.L. Doussal, Creep and depinning in disordered media, Phys. Rev. B Condens. Matter 62 (10) (2000) 6241–6267, https://doi.org/10.1103/physrevb.62.6241.
[37] P.J. Metaxas, et al., Creep and Flow Regimes of Magnetic Domain-Wall Motion in UltrathinPt/Co/PtFilms with Perpendicular Anisotropy, Phys. Rev. Lett. 99 (21) (2007) 217208, https://doi.org/10.1103/physrevlett.99.217208.
[38] D. Kato, et al., Fabrication of Magnetic Tunnel Junctions with Amorphous CoFeSiB Ferromagnetic Electrode for Magnetic Field Sensor Devices, Appl. Phys. Express 6 (10) (2013) 103004, https://doi.org/10.7567/apex.6.103004.